ADVANCED OPTICAL MATERIALS
www.advopticalmat.de

Hemispherical Rutile Solid Immersion Lens for Terahertz Microscopy with Superior 0.06–0.11λ Resolution

Vladislav A. Zhelnov, Nikita V. Chernomyrdin, Gleb M. Katyba, Arsenii A. Gavdush, Vladimir V. Bukin, Sergey V. Garnov, Igor E. Spektor, Vladimir N. Kurlov, Maksim Skorobogatiy, and Kirill I. Zaytsev*

Solid immersion microscopy is a near-field imaging modality that overcomes the Abbe diffraction limit by focusing the light beam behind a high refractive index lens. It offers high energy efficiency, thanks to the absence of any sub-wavelength probes or apertures in the optical path. A favorable combination of superresolution and high optical throughput opens up a variety of imaging applications in different branches of science and technology. The spatial resolution of solid immersion microscopy is mostly limited by the refractive index value of the lens, with optically denser lenses offering higher resolutions. In this paper, bulk rutile (TiO_2) crystal is used as a material for the solid immersion lens, which offers an impressive refractive index of ≈10 in the terahertz range. This is the highest value of refractive index ever used in solid immersion microscopy. A continuous wave impact ionization avalanche transit-time diode-emitter at the 0.2 THz frequency (the $\lambda = 1.5$ mm wavelength) and a Golay detector are used for building a solid immersion microscope. Numerical and experimental studies reveal 0.06–0.11λ resolution of the developed microscope. This is the highest normalized resolution ever reported for any solid immersion imaging systems.

1. Introduction

Solid immersion (SI) microscopy was originally introduced to overcome the $\simeq 0.5\lambda$ Abbe resolution limit of bulk optics in the visible range.[1] The essence of the SI effect is a reduction in the dimensions of the focal spot, when it is formed in free space, at a subwavelength ($<\lambda$) distance behind the flat surface of a high-refractive-index (RI) SI lens. In such lenses, the beam size is determined by the net contribution from both the propagating and evanescent waves, while the latter are excited at the lens—object flat interface due to the total internal reflection (TIR) phenomenon.[2] Compared to a regular lens, the focal spot size of an SI lens is reduced by a factor proportional to the SI lens RI.[2] Thus, using materials with high-to-moderate RIs (such as high-density glass, silicon, etc.) with a resolution as high as 0.15–0.5λ was demonstrated.[3] In addition to sub-wavelength resolution, SI microscopy also offers advanced energy efficiency when compared to other near-field imaging modalities. This is thanks to the absence of any sub-wavelength probes and apertures in the optical path. This allows implementing SI microscopes using common low-power emitters and uncooled detectors. For a detailed comparison of various subwavelength imaging modalities and a discussion of the comparative advantages of SI microscopy, refer to our recent review paper.[2]

To date, a variety of SI lenses have been developed exploiting different material platforms and fabrication strategies, geometries, and optical designs[2,4–9] from ultraviolet to terahertz (THz) spectral ranges. Moreover, SI microscopy was applied to solve many demanding fundamental and applied problems in super-resolution visible,[10] infrared (thermal)[11] and Raman[12] imaging, condensed matter physics and superconductivity,[13–16] quantum sciences,[17,18] data storage,[19] non-destructive evaluations,[20] biomedicine[21] and other disciplines.

Most recently, SI microscopy was translated into the THz range with frequencies in the $\nu \approx 10^{-1}$–10^{1} THz range.[22–24] In particular, our team developed the reflection-mode THz SI microscope,[25] using a SI THz lens comprised of a wide-aperture aspherical polymer singlet[26] and a high-resistivity silicon hemisphere with the THz RI of $n_{Si} \simeq 3.414$, negligible dispersion and absorption.[27] In turn, the silicon hemisphere is comprised of two mechanical elements—a rigidly-fixed hypohemisphere and a movable window, which are kept in contact and, thus, form a unitary optical element. Such a composite structure makes possible imaging of soft objects (including biological tissues) placed on

V. A. Zhelnov, N. V. Chernomyrdin, A. A. Gavdush, V. V. Bukin, S. V. Garnov, I. E. Spektor, K. I. Zaytsev
Prokhorov General Physics Institute of the Russian Academy of Sciences
Moscow 119991, Russia
E-mail: chernik-a@yandex.ru
G. M. Katyba, V. N. Kurlov
Osipyan Institute of Solid State Physics of the Russian Academy of Sciences
Chernogolovka 142432, Russia
M. Skorobogatiy
Department of Engineering Physics
Polytechnique Montreal
Montreal, Quebec H3C 3A7, Canada

The ORCID identification number(s) for the author(s) of this article can be found under https://doi.org/10.1002/adom.202300927

DOI: 10.1002/adom.202300927

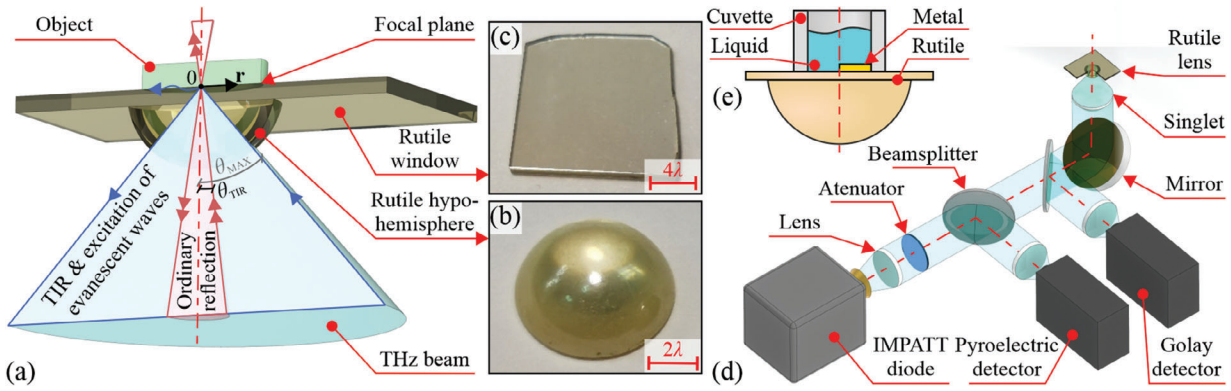

Figure 1. Reflection-mode continuous-wave THz SI microscope based on the composite rutile hemisphere. a) Schematic of the SI lens that comprises a wide-aperture aspherical polymer singlet (not shown), a rigidly-fixed rutile hypohemisphere and a movable rutile window that together form a proper hemisphere. b,c) Photos of the fabricated rutile hypohemisphere and window. d) Schematic of a THz SI microscope that uses a rutile-based SI lens, an IMPATT diode emitter, and a Golay detector. e) Schematic of the holder for measurement of the liquid test objects.

top of a movable window, which is raster-scanned with a focused THz beam.[3,25] Using the THz SI microscope with a silicon-based SI lens, the record-breaking 0.15λ resolution was achieved when imaging amplitude masks (with air-filled cutouts) placed in the SI lens shadow side[25]; while the dependence of the SI microscope resolution on the object RI and losses was studied in ref. [28]. Furthermore, the analytical and numerical models for the formation of a sub-wavelength beam spot by the SI lens were reported in ref. [29]. We then applied our THz SI microscope to visualize margins and heterogeneity of the glioma models from rats ex vivo,[29–31] as well as to study heterogeneous decellularized tissues during their interactions with a humid atmosphere.[32]

Up till now, further improvement of the SI microscopy resolution was hampered by the limited RIs of the naturally-occurring optically-transparent materials, which in the THz spectral range are typically lower than that of silicon $n \leqslant 3.0$–3.5. An interesting approach to increasing the lens RI was reported in refs. [10, 33], where composite SI lenses were fabricated either by self-assembly of the high-RI TiO_2 nanoparticles from colloidal suspension (for the visible range), or by pressing the mixture of TiO_2 and polymer micro-powders (for the THz range), respectively. In ref. [33], the THz RI of such a composite SI lens reached $n = 4$, but the resultant material suffered from high THz-beam attenuation due to absorption and scattering.

To further increase the resolution of SI microscopes, in this paper, a high-RI rutile (TiO_2) bulk crystal is studied, for the first time, as a novel material platform for SI lens fabrication in the THz range. We conduct both full-vectorial numerical simulations and experimental studies of SI imaging using the reflection-mode continuous-wave THz SI microscope operating at $\lambda = 1.5$ mm ($\nu \simeq 0.2$ THz). The results of our study confirm the superior 0.06–0.11λ resolution of the rutile-based THz SI lenses compared to any other previously reported SI lens material. Our findings pave the way for the use of rutile optics as a novel material platform for the superresolution THz microscopy.[34]

2. Design and Fabrication of the Rutile SI Lens

For this study, we chose the SI lens geometry shown in **Figure 1**a, which is similar to that detailed in ref. [25]. It features a wide-aperture aspherical polymer singlet,[26] and a composite hemisphere made of rutile. The singlet with a focal length of 15 mm and a diameter of 25 mm is illuminated by a collimated THz beam to form a convergent wavefront. The rutile hemisphere with a diameter of 10 mm and a thickness of 5 mm is mounted after a singlet so that its spherical surface is irradiated by the convergent wavefront, while its flat surface is coincident with the singlet focal plane. For such a SI lens geometry, no refraction is expected at the spherical surface of rutile hemisphere. The distance between the singlet and hemisphere is $\simeq 2.7$ mm. The rutile hemisphere serves as a resolution enhancer, with the sub-wavelength THz-beam caustic formed at its flat surface (i.e., an imaging plane).[2,25,29]

The composite rutile hemisphere is comprised of a 4-mm-thick rigidly-fixed hypohemisphere (Figure 1b) and a 1-mm-thick movable window (Figure 1c), which are kept in contact with no refraction between them. The movable rutile window serves as a sample holder and allows raster-scanning of the imaged objects with a focused THz beam. For the details of rutile optics fabrication, see the Experimental Section.

Since the optically-anisotropic dielectric response of a rutile crystal depends significantly on the crystal growth method and conditions,[35] our crystal (RusGems) is first characterized using the in-house THz pulsed spectrometer; see Experimental section. In particular, at $\lambda = 1.5$ mm ($\nu \simeq 0.2$ THz), the ordinary and extraordinary RIs of rutile were found to be $n^{o}_{TiO2} = 9.83$ and $n^{e}_{TiO2} = 13.58$, respectively, while the THz-wave absorption coefficient was estimated to be $\alpha_{TiO2} = 0.2\ \mathrm{cm}^{-1}$, by power. In Figure 1a, the rutile c-axis is oriented collinearly with the optical axis to minimize the effect of the crystal anisotropy on the focusing properties of a SI lens.

Figure 1d shows a schematic of the reflection-mode THz SI microscope, which is similar to its silicon-based counterpart.[3,25] The THz beam is first modulated at $\simeq 23$ Hz by a mechanical chopper, and then detected using a Golay cell (GPI RAS) aided by a lock-in detector to enhance the signal-to-noise ratio. Unlike in our previous works,[3,25] where a bulky backward-wave oscillator was used as a THz source, here we resort to a much smaller and portable continuous-wave impact ionization avalanche transit-time (IMPATT) diode-emitter (TeraSense Group),[36] with the

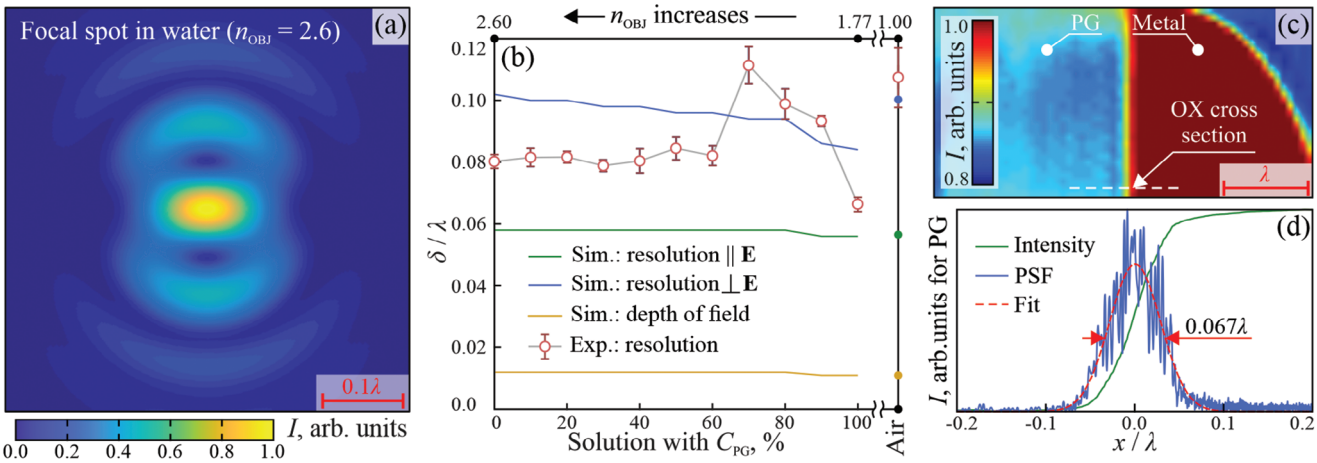

Figure 2. Comparison of the theoretical and experimental studies for the resolution of a rutile SI lens. a) 3D-FEFD intensity distribution at the planar interface of a SIL lens bordering water as an imaged object. b) Comparison of the SI lens resolutions for aqueous mixtures of PG as predicted by the 3D-FEFD and the experimentally-measured ones as a function of the PG concentration and RI. The 3D-FEFD predictions for the SI lens depth of field are also presented. c) THz microscopic image of a 100% PG–metal interface with an abrupt reflectivity change. d) Intensity profile estimated from the THz image in panel (c) and its first derivative, along with a smoothed fit, treated as a focal spot.

non-polarized output (the degree of polarization is $\simeq 0.7$), the output wavelength of $\lambda = 1.5$ mm ($\nu \simeq 0.2$ THz), and the beam power of 100 mW. However, due to poor long-term stability of the IMPATT output power (fluctuations of a few percent), which is comparable to the THz image contrast, an additional pyroelectric detector (also with lock-in) is used for continuous calibration of the THz beam power. Thus, for each measurement (pixel), the THz beam power scattered by a sample and detected by the Golay cell is normalized by that captured by the pyroelectric detector. The THz image was formed by raster scanning the object with the spatial step of the lateral window translations as small as 0.025λ, satisfying the Nyquist–Shannon–Kotelnikov sampling theorem.[37]

In Figure 1e, schematic of the liquid test sample confined by an inverted polymer cuvette atop a movable rutile window is shown. It makes possible imaging the liquid object-metal interfaces (i.e., "razor blade" method) to study the dependence of microscope resolution on the liquid object's optical properties.

3. Numerical and Experimental Studies of the SI Lens Resolution

Numerical simulation of the TiO_2 SI lens focusing properties was carried out using the 3D finite-element frequency-domain method (3D FEFD) which includes material anisotropy for rutile material as detailed in the Experimental Section. In ref. [29], we detailed how the focusing efficacy of an SI lens system featuring an axis of rotational symmetry can be analyzed using 3D-FEFD and assuming linearly polarized illumination. In **Figure 2**a, we present intensity distribution on the SI lens surface that borders with water as an imaged object with the RI and power loss of $n_{OBJ} = 2.6$ and $\alpha_{OBJ} = 100$ cm^{-1}, respectively, at 0.2 THz. In this case, the beam spot shape is strongly elliptical with dimensions of $\delta_y = 0.06\lambda$ and $\delta_x = 0.10\lambda$. In this simulation, the electric field polarization is along the OX axis, and δ is estimated as the full-width at half-maximum (FWHM) of the THz focal spot.

Generally, the use of optically-anisotropic wide-aperture focusing elements can change the polarization of incident wave and, thus, form a beam spot with a more complex (non-linear) polarization state. In our case, due to the choice of a crystal *c*-axis along the optical symmetry axis, the resultant SI lens geometry is axisymmetric. As a result, one can show theoretically using decomposition onto pure angular momentum Bessel beams, that when such a lens is excited with a linearly-polarized parallel beam propagating along the optical axis, the transverse fields in the focal beam spot are also linearly polarized. For details, see the theoretical calculations underlying the 3D FEFD method in the Experimental Section. One has to keep in mind that at the focal spot, there can also be a strong contribution of a longitudinal component of the electric field (directed along the optical axis) that might have a non-trivial angular dependence, which is also the case for SI lenses made of isotropic materials. Therefore, from the viewpoint of focal spot polarization, the anisotropic rutile-based THz SI lens studied in this paper works similarly to optically-isotropic SI lenses. This is also confirmed directly by the 3D FEFD method which allows a quasi-2D formulation even in the case of optically anisotropic axisymmetric systems as detailed in the Experimental Section. Therefore, any changes in polarization state of the THz beam spot and back-reflected wave result predominantly from the misalignment of the microscope optical elements and the direction of the rutile *c*-axis, as well as from wave scattering on the heterogeneities of the object under study.

Finally, we note that accounting for the birefringence of an SI lens material is not trivial, and should be ideally performed using fully vectorial 3D simulations. For isotropic materials (e.g., Si), the hemispherical geometry of an SI lens results in broadband operation when its spherical surface is concentric to the convergent spherical wavefront. For anisotropic materials (e.g., rutile) with a *c*-axis oriented along the optical symmetry axis, while one preserves rotational symmetry of the system, however, ordinary and extraordinary waves propagate inside the hemisphere with different group and phase velocities, thus, complicating the beam spot formation at the lens flat interface, and leading to potentially

frequency-dependent spot size, and high sensitivity to the lens geometry.

Since resolution and overall performance of SI optics is typically object-dependent,[28] in Figure 2b, the normalized resolution parameter δ is studied as a function of the object RI n_{OBJ}. To further verify the results of numerical simulations with experiment, we considered aqueous solutions of propylene glycol (PG), the RI, and losses of which decrease monotonically in the ranges of $n_{OBJ} = 2.6–1.77$ and $\alpha_{OBJ} = 100–5$ cm^{-1} when the PG concentration C_{PG} increases from 0% to 100% (by volume). The THz optical properties of these solutions, as found using the THz pulsed spectroscopy, are presented in the Experimental Section. As discussed in ref. [29], this range of material parameters is close to that of biological tissues and, thus, it is of particular importance for biomedical applications. From Figure 2b, we see that for these values of the object optical parameters the 3D-FEFD simulations predict anisotropic resolution of $\delta_y = 0.056–0.058\lambda$ and $\delta_x = 0.084–0.102\lambda$, assuming that the electric field **E** of an incident plane wave is directed along the OX axis.

Experimentally, a polymer cuvette is placed atop the rutile hemisphere, into which a metal blade is inserted at the base. The cuvette is either empty (air) or filled with different liquids, to form a dielectric-metal interface of tunable RI (see Figure 1e). Particularly, the PG aqueous solutions of different concentrations ($C_{PG} = 0.0–1.0$ by volume) are used as liquid, similarly to ref. [29]. In Figure 2b, we see that the experimental resolution is found to be $\delta = 0.115\lambda$ for air, and $\delta = 0.067–0.127\lambda$ for the PG aqueous solutions. As we used a non-polarized THz-wave emitter in our setup, the experimental resolution values fall expectedly in between the numerical curves predicted for the two orthogonal directions toward the linearly-polarized electric field **E**.

It is crucial to note that the predicted 1.5–2.0-fold difference in resolutions across the two orthogonal directions of the image plane is primarily attributed to the varying contributions of the axial (OZ) electric field in these two directions. If one calculates the intensity based on the transverse electric field components alone, the focal spot is almost perfectly circular with the size $\delta \simeq 0.06\lambda$. Therefore, object geometry and orientation can influence the experimentally-measured resolution, and further studies are still in order. Finally, in Figure 2, the 3D-FEFD method predicts a deeply subwavelength depth of field for our imaging system (i.e., the beam caustic size in the axial direction), which is about $\simeq 0.011\lambda$.

In **Table 1**, we summarize the resolution data of some notable optical systems that operate based on the SI effect across different ranges of the electromagnetic spectrum. In our analysis, we include only those SI lenses, which were characterized via common resolution criteria, such as Rayleigh's Airy disc radius, or the beam spot size at the FWHM level. We note that resolution of the THz rutile SI lens surpasses resolutions of all the previously developed THz SI lenses made of silicon for the THz range (see line 19 of Table 1), as well as all other lenses developed for the visible, near- and middle-infrared, and millimeter-wave ranges.

4. Deep Subwavelength Imaging with Rutile SI Lens

Rutile-based THz SI microscope is then applied to explore the limits of deep subwavelength imaging. In **Figure 3**a–f, we present photos and THz images of the 3D-printed logos of the GPI RAS, Polytechnique Montreal, and ISSP RAS (the institutions involved in this study). Logos of the GPI RAS and Polytechnique Montreal were made of the conductive compound of acrylonitrile butadiene styrene (ABS) polymer and carbon nanotubes with the resistivity of 4.64×10^2 Ω˜cm, while that of ISSP RAS - the polylactic acid (PLA) polymer. The depth of letters in all logos is 0.4 mm, which is much larger than the depth of field of our SI lens (Figure 2b). The width of letters is 0.4 mm or 0.27λ, being limited by the minimal diameter of a nozzle in our 3D printer (FlashForge Creator Pro 2). The sub-wavelength scale letters are clearly readable in all the THz images.

Additionally, in Figure 3g,h, we show photo and THz image of the stretchable Fresnel zone-plate formed via the carbon nanotubes deposition on a polymer film.[54] This THz optical element was developed and characterized in ref. [55]. From the THz image of this element, we also clearly observed distinct sub-wavelength scale Fresnel zones formed by conductive nanotubes. Therefore, our THz microscope can also image objects with variable electric conductivity (dielectric versus conductive regions) with impressive spatial resolution.

5. Discussion

The achieved record spatial resolution of the rutile-based THz SI microscope can find applications in different branches of THz science and technology. Among them, we particularly note medical diagnosis and biology,[31,56] non-destructive testing of materials,[57] and electronic circuits,[58] quality control in pharmaceutical[59] and food[60] industries.

At the same time, together with an impressive resolution come several challenges inherent to our system. First, the very high RI of rutile crystal greatly decreases the energy efficiency of our microscope, due to high Fresnel loss at the air-rutile interface. In principle, for narrow-band operation, this difficulty can be mitigated by employing an anti-reflection coating on the crystal surface. Second, due to high RI, a significant fraction of the THz beam aperture in our system undergoes TIR at the flat rutile-object interface (Figure 1a). Namely, with air on the shadow side of a SI lens, the critical TIR angle is only $\theta_{TIR} = \arcsin(n_{air}/n^{o}_{TiO2}) \simeq 6°$. This means that the response of our system is less sensitive to small variations in the object RI, as compared to SI lenses made of lower-RI materials, such as silicon.[29] Finally, we notice that, due to very high resolution and need for the rutile crystal *c*-axis to be oriented along the optical axis (to maintain the isotropic response of a microscope), the developed optical system demands more accurate fabrication and assembly as compared to the more standard THz SI microscopes that use lower-RI silicon lenses.[25]

Although in the present work we considered the THz SI microscopy in the continuous-wave reflection-mode modality, a transmission mode can also be realized.[24] Moreover, the thus developed THz SI microscope can be applied to quantitative imaging, that is for estimation of the object's optical properties at a given frequency.[29] Furthermore, a rutile lens can be combined with sources and detectors of THz pulses, thus, merging THz SI microscopy and THz pulsed spectroscopy for the detection of broadband spectra with sub-wavelength spatial resolution. However, one has to be aware of the rapid increase of rutile

Table 1. The spatial resolution of some representative SI lenses, where the items are sorted by increasing of resolution.

#	Resolution	Spectral range	Wavelength, λ	SI lens material	Ref.
1	0.49λ	THz	637 μm	Si	[38]
2	0.43λ	Near-infrared	0.83 μm	Glass	[39]
3	0.41λ	Visible–near-infrared	0.78 μm	Glass	[40]
4	0.4λ	Near-infrared	1.1–1.7 μm	Si	[41]
5	0.35λ	THz	500 μm	Si	[42]
6	0.34λ	Mid-infrared	5 μm	Si	[43]
7	0.33λ	Near-infrared	0.8–1.1 μm	Al_2O_3	[44]
8	0.31λ	Near-infrared	0.815 μm	ZrO_2	[45]
9	0.3λ	Millimeter-wave	1500–3000 μm	Al_2O_3	[46]
10	0.28λ	Mid-infrared	5 μm	Si	[47]
11	0.28λ	Visible	0.6328 μm	LaSFN9 glass	[48]
12	0.23λ	Mid-infrared	10.7 μm	Si	[49]
13	0.23λ	Visible	0.436 μm	Glass	[1]
14	0.21λ	Near-infrared	1.53 μm	Si	[50]
15	$0.2–0.3\lambda$	THz	3.3 mm	TiO_2/PP	[33]
16	$0.2–0.23\lambda$	Mid-infrared	9.3–10.7 μm	Si	[51]
17	0.2λ	Mid-infrared	9.3 μm	Si	[52]
18	$0.15–0.31\lambda$	Near-infrared	1.2 μm	Si	[53]
19	0.15λ	THz	500 μm	Si	[25]

material loss and dispersion at higher THz frequencies, as shown in the Experimental Section. Rutile lens can also be implemented in various other designs, such as hyper-hemispherical super-SI lens (Weirstrass lens),[21] diffractive,[5] microfabricated,[4,12] and endoscopic[61] SI lenses. All these arrangements and schemes are to be used for alternative implementations of super-resolution THz microscopy.

6. Conclusions

In this work, we investigated both numerically and experimentally the rutile (TiO_2) SI lens having the impressive RI of ≈10 at THz frequencies for applications in superresolution microscopy. Our theoretical and experimental findings revealed that rutile SI lens enables a record-breaking (for SI optics) spatial resolution of $0.06–0.11\lambda$, which is 5–10 times lower than the ≃ 0.5 Abbe diffraction limit of free space optics. Such a high resolution represents considerable advancement over all the prior-reported SI lenses in all the spectral ranges from the visible to the microwave. Our findings pave the way for new generation of rutile-based SI optics in super-resolution THz imaging.

7. Experimental Section

Fabrication of the Rutile Optics: A cube with the dimensions of 11 × 11 × 11 mm^3 was cut out of the rutile crystal (came from the RusGem, Russia) (see **Figure 4**a). It was rounded into a sphere with the diameter of 10 mm (see Figure 4b), which was then polished using a diamond powder and a bowl made of beech with the spherical surface coated by a velvet. This sphere was cut into a 5-mm-thick hemisphere and a 4-mm-thick hypohemisphere, with the polished flat surfaces and the rutile *c*-axis directed along the optical axis; see Figure 4c,d, respectively.

A 1-mm-thick rutile window with the surface area of ≃ 3 cm^2 and the rutile *c*-axis in the direction of the optical axis was cut off the bulk crystal, grinded, and polished from both sides; see Figure 4e. Together with the 4-mm-thick hypohemisphere, this window forms a unitary hemispherical rutile lens with the total thickness of 5 mm. Another 1-mm-thick window with a similar surface area, and the rutile *c*-axis in plane of optical surfaces was cut off the bulk crystal for further spectroscopic characterization of the anisotropic THz dielectric response of our rutile crystal.[35]

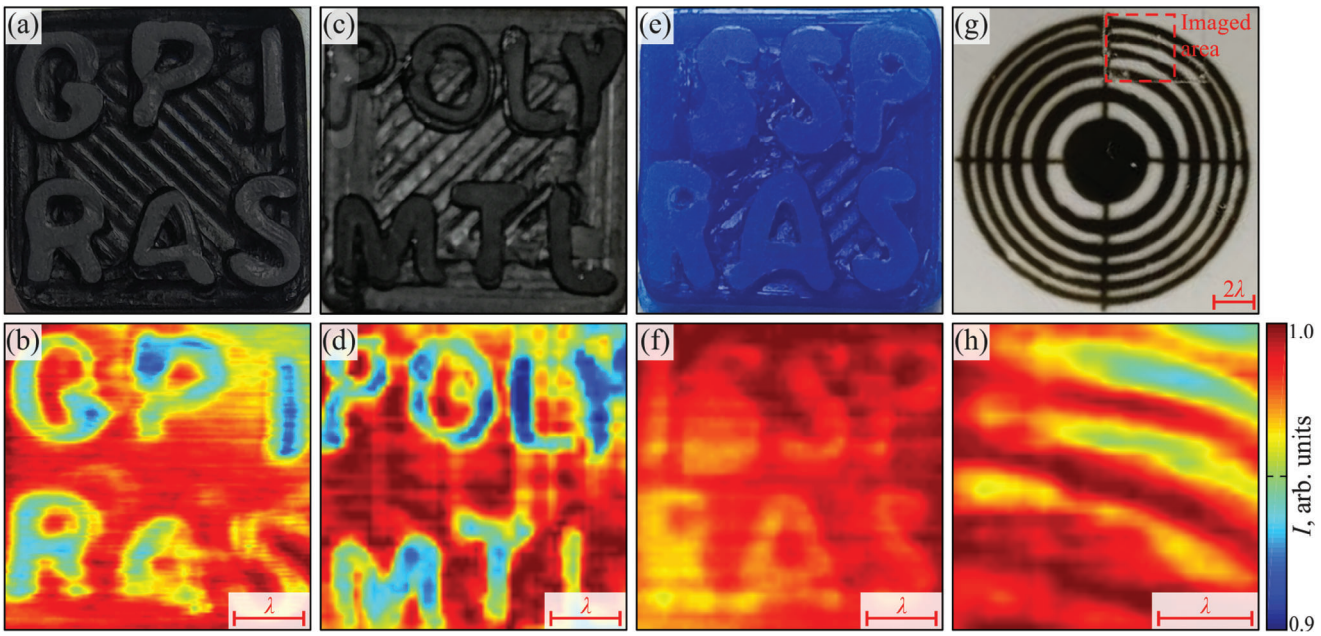

Figure 3. THz SI microscopy of objects with subwavelength features. a–f) Photos and THz images of the 3D-printed polymer logos of GPI RAS and Polytechnique Montreal (both are made of the conductive ABS polymer), as well as ISSP RAS (PLA polymer). g,h) Photo of the stretchable carbon nanotubes-based THz Fresnel zone-plate, reported in ref. [55], and THz image of its fragment, respectively.

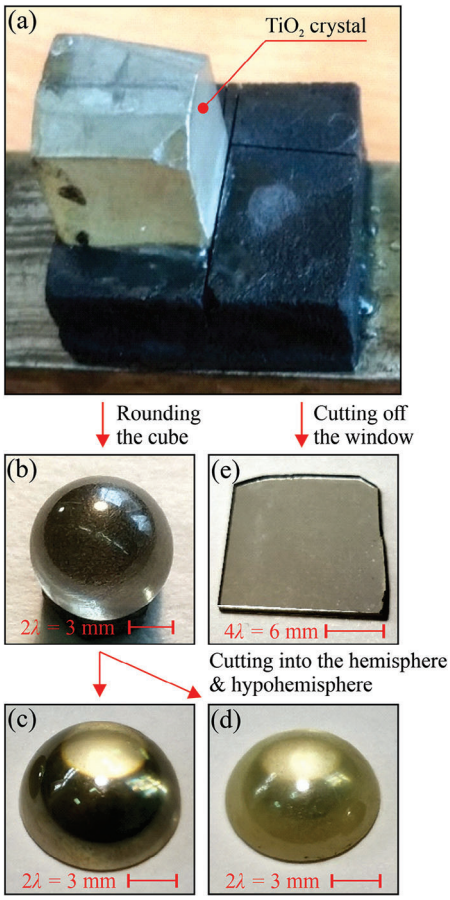

Figure 4. Fabrication of the TiO_2 hypohemisphere and window. a) A photo that illustrates cutting a cube with the dimensions of $11 \times 11 \times 11$ mm^3 from a bulk rutile crystal. b) A photo of the 10-mm-diameter rutile sphere obtained from the cube by mechanical rounding, grinding, and polishing. c,d) Photos of the rutile hemisphere and hypohemisphere cut from the sphere and polished. e) A photo of the 1-mm-thick rutile window cut of a bulk crystal, grinded and polished. In the scale bars, $\lambda = 1.5$ mm ($\nu \simeq 0.2$ THz) corresponds to the operation wavelength of our THz microscope.

Finally, a wide-aperture aspherical polymer singlet,[26] a rutile hypohemisphere, and a rutile window were assembled into the desired SI lens as detailed in the main manuscript text and refs. [3, 25].

THz Pulsed Spectroscopy of Rutile: In order to study the anisotropic THz optical properties of rutile crystal, an in-house transmission-mode THz pulsed spectrometer was used, that relied on a pair of photoconductive antennas, as an emitter and detector of THz pulses. It had a vacuumized THz beam path, that prevented an impact of the water vapor in a humid atmosphere on the measured THz data and extended the spectral range of the sample characterization. It was also equipped with a pair of the free-standing metal-grid polarizers, aimed of the polarization-sensitive THz measurements.[62–64]

To retrieve the THz optical properties of the rutile window, an approach detailed in refs. [65, 66] was used. In **Figure 5**, the measured refractive indices n and absorption coefficients α (by power) are shown for the ordinary and extraordinary rays of a rutile crystal in the 0.1–0.8 THz range. The measurement bandwidth was limited by both the detector sensitivity and a high Fresnel loss at the free-space–rutile interfaces. A red dashed curve in Figure 5, corresponds to the 0.2 THz working frequency (the $\lambda = 1.5$ mm wavelength) of the THz SI microscope. At this frequency, the ordinary and extraordinary RIs of rutile were as high as $n^{o}_{TiO2} = 9.83$ and $n^{e}_{TiO2} = 13.58$, respectively, while its absorption coefficients were relatively small ($\alpha_{TiO2} <$ 0.5 cm^{-1}, by power), for the considered thicknesses of the rutile optical elements. These optical constants of rutile were used in numerical analysis of our SI lens.

Numerical Modeling of the SI Lens: Numerical modeling of the developed SI lens, which included both an aspherical singlet and a composite SI hemisphere, was carried out using the 3D FEFD method[67] within the COMSOL Multiphysics Software.

Axial symmetry of the SI lens allowed the reduction of a 3D problem to a quasi-2D in cylindrical coordinates with a rotational symmetry axis directed along the main optical axis. The 3D FEFD modeling was performed using a 2D cross-section of an optical system in cylindrical coordinates. Cylindrical perfectly matched layers were applied at the boundaries of a computational volume to suppress non-physical back-scattering of the electromagnetic waves. Two circularly polarized plane waves with the wavelength of $\lambda = 1.5$ mm and angular momenta of $m = \pm 1$ were introduced into the simulation volume using the total-field/scattered-field approach. Thus, obtained two sets of solution fields were then coherently added, to get a solution that corresponded to a linearly-polarized plane wave excitation field.

In these simulations, the rutile c-axis to be directed along the optical axis of the system was considered and the experimentally-obtained ordinary $n^{o}_{TiO2} = 9.83$ and extraordinary $n^{e}_{TiO2} = 13.58$ refractive indices of rutile at 0.2 THz ($\lambda = 1.5$ mm) were used, while for both ordinary and extraordinary rays, the THz absorption coefficient was set to $\lambda_{TiO2} = 0.5$ cm^{-1} (by power). Spatial distribution of the THz-field intensity in a modeled 3D space was calculated as $I(\mathbf{r}) \propto |\mathbf{E}(\mathbf{r})|^2$, where $\mathbf{r}$ is a 3D radius vector. Panel (a) in **Figure 6** corresponds to the axial cross section of an optical system, which is collinear to the optical axis and the electric field vector $\mathbf{E}$. In (b), intensity distribution over the focal (object) plane is shown, defining the focal spot geometry (point spread function) of this system. Note that thus presented numerical data corresponded to water at the SI lens shadow side.

The THz beam spot sizes were calculated as FWHM of the intensity distributions at the flat surface of a hemisphere from the air side. In Figure 6b, the electric field vector was directed along the OX-axis, while the beam spot sizes along OX and OY and, thus, the resultant resolution parameters are as small as $\delta_{OX} = 0.10\lambda$ and $\delta_{OY} = 0.06\lambda$, respectively.

Details of the Quasi-3D Numerical Analysis for the Linear Polarized Modes: Consider a vector amplitude of a plane wave source in the Cartesian coordinates $\mathbf{E}_{Cart} = (E_x, E_y, E_z)$. Particularly, for the OX-polarized unit-amplitude plane wave

$$\mathbf{E}^{PW,\ PolOX}_{Cart} = (1, 0, 0) \tag{1}$$

Cylindrical coordinate system $\mathbf{E} = (E_\rho, E_\theta, E_z)$ was now resorted by using the following transformations:

$$E_\rho = E_x \cos(\theta) + E_y \sin(\theta),\ E_\theta = -E_x \sin(\theta) + E_y \cos(\theta) \tag{2}$$

In the Cylindrical coordinate system, the OX polarized unit-amplitude plane wave becomes

$$\mathbf{E}^{PW,\ PolOX}_{Cyl} = (\cos(\theta), -\sin(\theta), 0) = \frac{1}{2}\left((1, i, 0)\exp(i\phi) + (1, -i, 0)\exp(-i\phi)\right) \tag{3}$$

where $(1, i, 0)\exp(i\phi)$ and $(1, -i, 0)\exp(-i\phi)$ are states with the angular momentum of $m = 1$ and $m = -1$, correspondingly. Therefore, in the cylindrical coordinates, an incoming OX-polarized plane wave that propagates along the OZ-direction (along the optical axis) could be represented as a superposition of the two pure angular momentum states, $m \pm 1$.

Simulation was performed via the COMSOL Multiphysics Software using the total-field/scattered-field approach to introduce the ideally-plane wave into the simulated volume and the OZ rotational symmetry axis. The native coordinate system for this calculation was a cylindrical one. As a

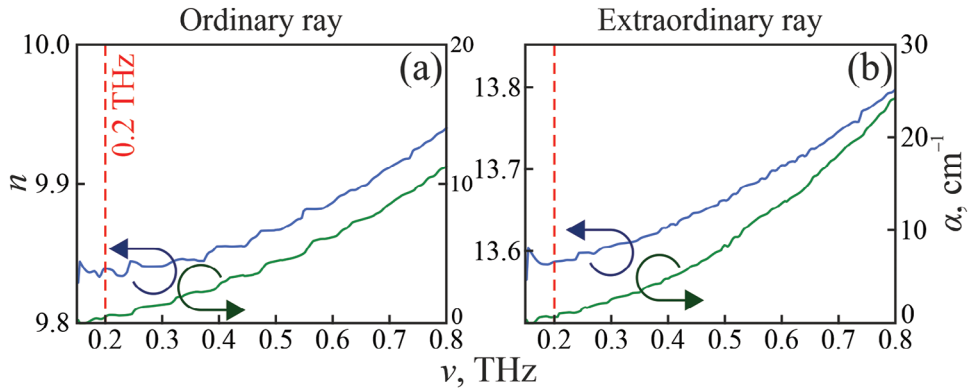

Figure 5. THz refractive index n and absorption coefficient α (by power) of the rutile crystal for a) ordinary and b) extraordinary rays. The vertical red-colored dashed line shows the frequency of 0.2 THz, at which our THz microscope operates.

source, a plane wave with a pure $m = 1$ state was used, which in the Cylindrical coordinates has the form

$$\mathbf{E}_{\text{Cyl}}^{\text{Source},\, m=1} = (1, i, 0)\exp(i\theta) \tag{4}$$

As a result of simulations, electromagnetic fields were retrieved in a pure $m = 1$ state

$$\begin{aligned}\mathbf{E}_{\text{Cyl}}^{\text{Sol},\, m=1} &= \left(e_\rho^1(\rho,z), e_\theta^1(\rho,z), e_z^1(\rho,z)\right)\exp(i\theta),\\ \mathbf{H}_{\text{Cyl}}^{\text{Sol},\, m=1} &= \left(h_\rho^1(\rho,z), h_\theta^1(\rho,z), h_z^1(\rho,z)\right)\exp(i\theta)\end{aligned} \tag{5}$$

Next, a plane wave with a pure $m = -1$ state was used as a source, which in cylindrical coordinates is given by

$$\mathbf{E}_{\text{Cyl}}^{\text{Source},\, m=-1} = (-1, i, 0)\exp(-i\theta) \tag{6}$$

After simulations, electromagnetic fields were retreived in a pure $m = -1$ state:

$$\begin{aligned}\mathbf{E}_{\text{Cyl}}^{\text{Sol},\, m=-1} &= \left(e_\rho^{-1}(\rho,z), e_\theta^{-1}(\rho,z), e_z^{-1}(\rho,z)\right)\exp(-i\theta),\\ \mathbf{H}_{\text{Cyl}}^{\text{Sol},\, m=-1} &= \left(h_\rho^{-1}(\rho,z), h_\theta^{-1}(\rho,z), h_z^{-1}(\rho,z)\right)\exp(-i\theta)\end{aligned} \tag{7}$$

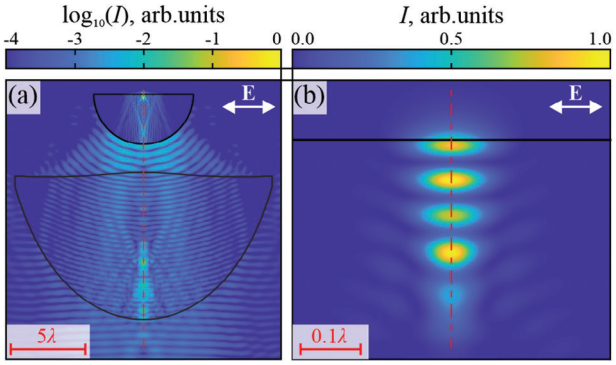

Figure 6. Numerical 3D FEFD estimation of the electric field intensity distribution $I(\mathbf{r}) \propto |\mathbf{E}(\mathbf{r})|^2$ in a) the axial cross-section and b) the focal/object plane of the SI lens, with a free space at its shadow side.

Note that, in fact, there was no need to recalculate the fields for the $m = -1$ state, as they could be found analytically from the fields of the $m = 1$ state due to the axial symmetry:

$$\begin{aligned}\left(e_\rho^{-1}(\rho,z), e_\theta^{-1}(\rho,z), e_z^{-1}(\rho,z)\right) &= \left(e_\rho^1(\rho,z), -e_\theta^1(\rho,z), e_z^1(\rho,z)\right),\\ \left(h_\rho^{-1}(\rho,z), h_\theta^{-1}(\rho,z), h_z^{-1}(\rho,z)\right) &= \left(-h_\rho^1(\rho,z), h_\theta^1(\rho,z), -h_z^1(\rho,z)\right)\end{aligned} \tag{8}$$

which follows directly from the Maxwell's equations.

As follows from (3), fields due to the scattering of an OX polarized wave in Cylindrical coordinates are given by:

$$\begin{aligned}\mathbf{E}_{\text{Cyl}}^{\text{Sol, PolOX}} &= \frac{1}{2}\left(\mathbf{E}_{\text{Cyl}}^{\text{Sol},\, m=1} + \mathbf{E}_{\text{Cyl}}^{\text{Sol},\, m=-1}\right),\\ \mathbf{H}_{\text{Cyl}}^{\text{Sol, PolOX}} &= \frac{1}{2}\left(\mathbf{H}_{\text{Cyl}}^{\text{Sol},\, m=1} + \mathbf{H}_{\text{Cyl}}^{\text{Sol},\, m=-1}\right).\end{aligned} \tag{9}$$

Particularly, for electric field, it was found

$$\begin{aligned}\mathbf{E}_{\text{Cyl}}^{\text{Sol, PolOX}} &= \frac{1}{2}\left(\mathbf{E}_{\text{Cyl}}^{\text{Sol},\, m=1} + \mathbf{E}_{\text{Cyl}}^{\text{Sol},\, m=-1}\right)\\ &= \frac{1}{2}\left(\left(e_\rho^1(\rho,z), e_\theta^1(\rho,z), e_z^1(\rho,z)\right)\exp(i\theta)\right.\\ &\left.+\left(e_\rho^1(\rho,z), -e_\theta^1(\rho,z), e_z^1(\rho,z)\right)\exp(-i\theta)\right)\\ &= \left(e_\rho^1(\rho,z)\cos(\theta), ie_\theta^1(\rho,z)\sin(\theta), e_z^1(\rho,z)\cos(\theta)\right).\end{aligned} \tag{10}$$

Finally, by making a coordinate transformation back into the Cartesian system:

$$\begin{aligned}E_x &= E_\rho\cos(\theta) - E_\theta\sin(\theta),\\ E_y &= E_\rho\sin(\theta) + E_\theta\cos(\theta)\end{aligned} \tag{11}$$

and using Equation (10), the field of a scattered OX-polarized plane wave was found in terms of the fields found in COMSOL simulations

$$\mathbf{E}_{\text{Cart}}^{\text{Sol, PolOX}} = \left(E_x^{\text{Sol, PolOX}}, E_y^{\text{Sol, PolOX}}, E_z^{\text{Sol, PolOX}}\right) \tag{12}$$

where

$$E_x^{\text{Sol, PolOX}} = e_\rho^1(\rho, z)\cos^2(\theta) - ie_\theta^1(\rho, z), \sin^2(\theta)$$
$$= \frac{1}{2}\left(e_\rho^1(\rho, z) - ie_\theta^1(\rho, z)\right) + \frac{1}{2}\left(e_\rho^1(\rho, z) + ie_\theta^1(\rho, z)\right)\cos(2\theta),$$
$$E_y^{\text{Sol, PolOX}} = \frac{1}{2}\left(e_\rho^1(\rho, z) + ie_\theta^1(\rho, z)\right)\sin(2\theta), \quad (13)$$
$$E_z^{\text{Sol, PolOX}} = e_z^1(\rho, z)\cos(\theta)$$

The electric field intensity distribution could also be calculated in the Cartesian coordinate system

$$I_{\text{Cart}}^{\text{Sol, PolOX}} = \left|E_x^{\text{Sol, PolOX}}\right|^2 + \left|E_y^{\text{Sol, PolOX}}\right|^2 + \left|E_z^{\text{Sol, PolOX}}\right|^2$$
$$= \left(\left|e_\rho^1(\rho, z)\right|^2 + \left|e_z^1(\rho, z)\right|^2\right)\cos^2(\theta) + \left|e_\theta^1(\rho, z)\right|^2\sin^2(\theta) \quad (14)$$

As the E_x component has a dominant angle-independent contribution, in this sense, the transverse fields could be considered as OX polarized. At the same time, it was important to understand the full-vectorial nature of the fields to draw the proper conclusions. Also note that all the field components were included in the calculation of intensity. It was also observed that the strong asymmetry of the beam spot shape in Figure 6b comes from a contribution of the OZ electric field component. If not for the OZ component, the intensity distribution would be almost isotropic.

Finally, it was stressed that Equations (1)–(14) justify theoretically the linear polarization of the focal spot transverse fields formed by the THz SI lens, or by any other optical system with an axial symmetry.

THz Pulsed Spectroscopy of PG Aqueous Solutions: PG and its aqueous solutions were used in this study for the fabrication of test objects applied to examine the resolution and reflectivity of the SI lens; for the details, see the main manuscript text or ref. [29]. PG and its aqueous solutions were common hyperosmotic agents in the immersion optical clearing of tissues in the visible, infrared, and even THz bands.[68–70] In refs. [64, 71], their optical properties were studied (among other liquids), aimed at selecting the optimal agents for the tissue immersion optical clearing in the THz range.

To prepare solutions, pure PG (came from ChemicalLine, Russia) and deionized water (obtained by the HLP Hydrolab, Poland) were used. Aqueous solutions of PG were prepared by mixing the pure PG and deionized water using the volume/volume method. Then, THz optical properties of liquids were studied experimentally using the abovementioned in-house transmission-mode THz pulsed spectrometer, aided by judiciously-designed equipment and data processing routine.[62–64]

In **Figure 7**, the measured refractive indices n and absorption coefficients α (by power) were given for the analyzed liquids, which agree with our earlier-reported data.[29,64,71] It was noticed that both refractive index and absorption coefficient increased monotonically and almost linearly with a decrease of PG content in a solution. Particularly, at 0.2 THz, the refractive index n increased from 1.77 (for pure PG, 100%), to 2.60 (for deionized water). This yielded a wide tunability of the THz optical properties of a test object during the experimental studies of the SI lens resolution and reflectivity.

THz SI Microscopy of the Liquid Test Objects: These liquid samples were then applied to study the performance of the THz SI microscope. For this, test samples were placed atop the SI lens. They form a lateral dielectric–metal interface with abrupt reflectivity changes and a variable refractive index of a dielectric medium. This interface was formed by a metal (duralumin) plate placed in contact with a liquid inside a polymer cuvette atop of the rutile window; see the main manuscript text.

In **Figure 8**, the THz SI microscopic images of the test samples are shown. From these images, it was noticed that reflectivity of the metal plate was much higher than that of dielectric media. Next, in **Figure 9**, estimation of the SI system spatial resolution, as a function of the refractive index of an images object are illustrated. For this, point spread function of an optical system was estimated as a first derivative of the intensity

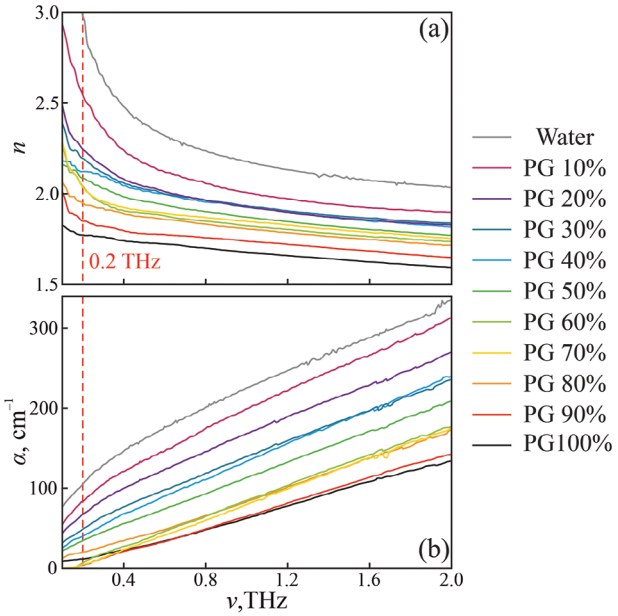

Figure 7. THz refractive index n (a) and absorption coefficient α (by power) (b) of the deionized water, PG (100%), and its aqueous solutions with the concentrations of 10–90% (by volume). The vertical red-colored dashed line shows the 0.2 THz frequency of our THz microscope operation.

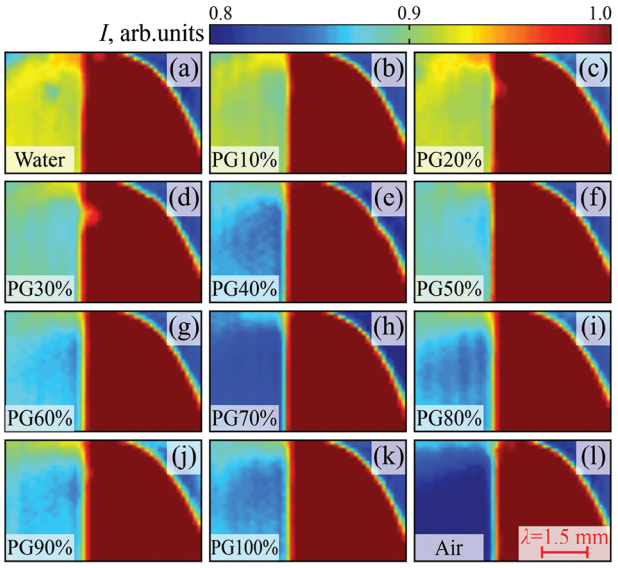

Figure 8. 0.2 THz (λ = 1.5 mm) SI microscopy of the test samples in the form of the dielectric–metal interfaces with abrupt reflectivity changes and distinct refractive indices of a dielectric medium. a) An image of the water–metal interface. b–l) Similar data for the 10–90% PG aqueous solutions (by volume) and air, respectively, in place of a dielectric medium.

profile, that was transverse to the dielectric–metal edge, and the resolution parameter δ was calculated as the point spread function FWHM. A superior spatial resolution is evident from our estimates, along with its object-dependent character, while the latter agrees with ref. [28].

Estimation of the Point Spread Function of an Optical System Based on Images of a Test Object with Abrupt Reflectivity Changes: Consider an

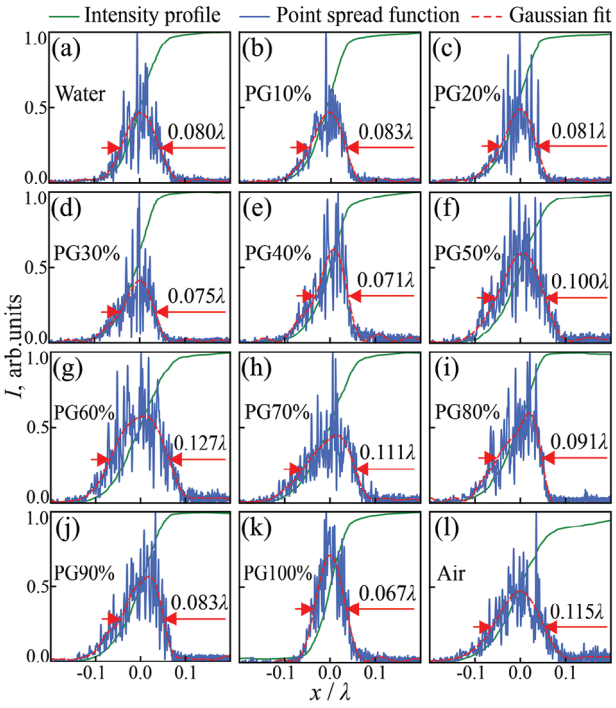

Figure 9. Estimation of the object-dependent 0.2 THz ($\lambda = 1.5$ mm) SI microscopy resolution from the images of test objects with dielectric–metal interfaces. a) Cross-section of the THz image $I(x)$ in the direction transverse to the water–metal interface (green curve), its first derivative $dI(x)/dx$ considered as the point spread function of an optical system (blue), as well as its smoothed polynomial fit (red), where the resolution is estimated at the FWHM level. b–l) Similar data for the 10–90% PG aqueous solutions (by volume) and air, respectively, in place of a dielectric medium.

object with reflectivity profile defined by the Heaviside step function in the OX direction

$$H(x) = \begin{cases} 0 & x < 0, \\ 1 & x \geq 0 \end{cases} \tag{15}$$

An image (an intensity profile) of such a 1D object can be defined via the convolution between the Heaviside function $H(x)$ and the point spread function (beam spot) $\mathrm{PSF}(x)$ of an optical system

$$I(x) \propto \mathrm{PSF}(x) \otimes H(x) = \int_{-\infty}^{\infty} \mathrm{PSF}(x')H(x-x')\mathrm{d}x' \tag{16}$$

Considering that the Heaviside function is an antiderivative of the Dirac δ-function and using the δ-function filtrating property, the following relation between the intensity profile derivative $dI(x)/dx$ and the point spread function $\mathrm{PSF}(x)$ can be obtained

$$\begin{aligned} \frac{dI(x)}{dx} &\propto \frac{d}{dx}\int_{-\infty}^{\infty} \mathrm{PSF}(x')H(x-x')dx' \\ &= \int_{-\infty}^{\infty} \mathrm{PSF}(x')\frac{dH(x-x')}{dx}dx' \\ &= \int_{-\infty}^{\infty} \mathrm{PSF}(x')\frac{d}{dx}(\delta(x-x')dx)dx' \\ &= \int_{-\infty}^{\infty} \mathrm{PSF}(x')\delta(x-x')dx' = \mathrm{PSF}(x) \otimes \delta(x) = \mathrm{PSF}(x) \end{aligned} \tag{17}$$

In this way, the first derivative of the intensity profile $dI(x)/dx$ can be treated as the point spread function of an optical system.

Acknowledgements

The work of V.A.Z., N.V.C., and K.I.Z. on the development, experimental implementation, and characterization of the rutile THz SI lens and related THz SI microscope was supported by the Russian Science Foundation, Project # 22–79–10099. The work of M.S. on the design and numerical modeling of the rutile THz SI lens was supported by the Ubiquitous Terahertz Photonics Project within the Canada Research Chairs Program. The authors are thankful to Nikita I. Raginov, Dmitriy V. Krasnikov, and Albert G. Nasibulin (Skolkovo Institute of Science and Technology) for their assistance with fabrication of the stretchable THz zone plate based on the carbon nanotubes.

Conflict of Interest

The authors declare no conflict of interest.

Data Availability Statement

The data that support the findings of this study are available from the corresponding author upon reasonable request.

Keywords

high refractive index, near-field microscopy, rutile, solid immersion microscopy, superresolution, terahertz optical materials, terahertz technology

Received: April 19, 2023
Revised: June 15, 2023
Published online: November 8, 2023

[1] S. Mansfield, G. Kino, *Appl. Phys. Lett.* **1990**, *57*, 2615.
[2] N. Chernomyrdin, M. Skorobogatiy, D. Ponomarev, V. Bukin, V. Tuchin, K. Zaytsev, *Appl. Phys. Lett.* **2022**, *120*, 110501.
[3] N. Chernomyrdin, V. Zhelnov, A. Kucheryavenko, I. Dolganova, G. Katyba, V. Karasik, I. Reshetov, K. Zaytsev, *Opt. Eng.* **2019**, *59*, 061605.
[4] D. Fletcher, K. Crozier, C. Quate, G. Kino, K. Goodson, D. Simanovskii, D. Palanker, *Appl. Phys. Lett.* **2000**, *77*, 2109.
[5] R. Brunner, M. Burkhardt, A. Pesch, O. Sandfuchs, M. Ferstl, S. Hohng, J. White, *J. Opt. Soc. Am. A* **2004**, *21*, 1186.
[6] I. Golub, *Opt. Lett.* **2007**, *32*, 2161.
[7] M.-S. Kim, T. Scharf, M. Haq, W. Nakagawa, H. Herzig, *Opt. Lett.* **2011**, *36*, 3930.
[8] D. Kang, C. Pang, S. M. Kim, H. S. Cho, H. S. Um, Y. W. Choi, K. Suh, *Adv. Mater.* **2012**, *24*, 1709.
[9] T.-Y. Huang, R. Grote, S. Mann, D. Hopper, A. Exarhos, G. Lopez, G. Kaighn, E. Garnett, L. Bassett, *Nat. Commun.* **2019**, *10*, 2392.
[10] W. Fan, B. Yan, Z. Wang, L. Wu, *Sci. Adv.* **2016**, *2*, e1600901.
[11] S. Ippolito, S. Thorne, M. Eraslan, B. Goldberg, M. Unlu, Y. Leblebici, *Appl. Phys. Lett.* **2004**, *84*, 4529.
[12] G. Lerman, A. Israel, A. Lewis, *Appl. Phys. Lett.* **2006**, *89*, 223122.
[13] Q. Wu, R. Grober, D. Gammon, D. Katzer, *Phys. Rev. Lett.* **1999**, *83*, 2652.
[14] Z. Liu, B. Goldberg, S. Ippolito, A. Vamivakas, M. Unlu, R. Mirin, *Appl. Phys. Lett.* **2005**, *87*, 071905.

[15] R. Hadfield, P. Dalgarno, J. O'Connor, E. Ramsay, R. Warburton, E. Gansen, B. Baek, M. Stevens, R. Mirin, S. Nam, *Appl. Phys. Lett.* **2007**, *91*, 241108.
[16] A. Bogucki, L. Zinkiewicz, M. Grzeszczyk, W. Pacuski, K. Nogajewski, T. Kazimierczuk, A. Rodek, J. Suffczyński, K. Watanabe, T. Taniguchi, P. Wasylczyk, M. Potemski, P. Kossacki, *Light: Sci. Appl.* **2020**, *9*, 48.
[17] T. Schroder, F. Gadeke, M. Banholzer, O. Benson, *New J. Phys.* **2011**, *13*, 055017.
[18] V. Devaraj, J. Baek, Y. Jang, H. Jeong, D. Lee, *Opt. Express* **2016**, *24*, 8045.
[19] B. Terris, H. Mamin, D. Rugar, W. Studenmund, G. Kino, *Appl. Phys. Lett.* **1994**, *65*, 388.
[20] S. Ippolito, P. Song, D. Miles, J. Sylvestri, *Appl. Phys. Lett.* **2008**, *92*, 101109.
[21] L. Wang, B. Bateman, L. Zanetti-Domingues, A. Moores, S. Astbury, C. Spindloe, M. Darrow, M. Romano, S. Needham, K. Beis, D. Rolfe, D. Clarke, M. Martin-Fernandez, *Commun. Biol.* **2019**, *2*, 74.
[22] A. Pimenov, A. Loidl, *Appl. Phys. Lett.* **2003**, *83*, 4122.
[23] B. Gompf, M. Gerull, T. Müller, M. Dressel, *Infrared Phys. Technol.* **2006**, *49*, 128.
[24] N. Chernomyrdin, A. Schadko, S. Lebedev, V. Tolstoguzov, V. Kurlov, I. Reshetov, I. Spektor, M. Skorobogatiy, S. Yurchenko, K. Zaytsev, *Appl. Phys. Lett.* **2017**, *110*, 221109.
[25] N. Chernomyrdin, A. Kucheryavenko, G. Kolontaeva, G. Katyba, I. Dolganova, P. Karalkin, D. Ponomarev, V. Kurlov, I. Reshetov, M. Skorobogatiy, V. Tuchin, K. Zaytsev, *Appl. Phys. Lett.* **2018**, *113*, 111102.
[26] N. Chernomyrdin, M. Frolov, S. P. Lebedev, I. V. Reshetov, I. E. Spektor, V. L. Tolstoguzov, V. E. Karasik, A. M. Khorokhorov, K. I. Koshelev, A. O. Schadko, S. O. Yurchenko, K. I. Zaytsev, *Rev. Sci. Instrum.* **2017**, *88*, 014703.
[27] D. Grischkowsky, S. Keiding, M. van Exter, C. Fattinger, *J. Opt. Soc. Am. B* **1990**, *7*, 2006.
[28] V. Zhelnov, K. Zaytsev, A. Kucheryavenko, G. Katyba, I. Dolganova, D. Ponomarev, V. Kurlov, M. Skorobogatiy, N. Chernomyrdin, *Opt. Express* **2021**, *29*, 3553.
[29] N. Chernomyrdin, M. Skorobogatiy, A. Gavdush, G. Musina, G. Katyba, G. Komandin, A. Khorokhorov, I. Spektor, V. Tuchin, K. Zaytsev, *Optica* **2021**, *8*, 1471.
[30] A. Kucheryavenko, N. Chernomyrdin, A. Gavdush, A. Alekseeva, P. Nikitin, I. Dolganova, P. Karalkin, A. Khalansky, I. Spektor, M. Skorobogatiy, V. Tuchin, K. Zaytsev, *Biomed. Opt. Express* **2021**, *12*, 5272.
[31] N. Chernomyrdin, G. Musina, P. Nikitin, I. Dolganova, A. Kucheryavenko, A. Alekseeva, Y. Wang, D. Xu, Q. Shi, V. Tuchin, K. Zaytsev, *Opto-Electron. Adv.* **2023**, *6*, 220071.
[32] G. R. Musina, N. V. Chernomyrdin, E. R. Gafarova, A. A. Gavdush, A. J. Shpichka, G. A. Komandin, V. B. Anzin, E. A. Grebenik, M. V. Kravchik, E. V. Istranova, I. N. Dolganova, K. I. Zaytsev, P. S. Timashev, *Biomed. Opt. Express* **2021**, *12*, 5368.
[33] Q. Chapdelaine, K. Nallappan, Y. Cao, H. Guerboukha, N. Chernomyrdin, K. Zaytsev, M. Skorobogatiy, *Opt. Mater. Express* **2022**, *12*, 3015.
[34] H. Guerboukha, K. Nallappan, M. Skorobogatiy, *Adv. Opt. Photonics* **2018**, *10*, 843.
[35] F. Gervais, B. Piriou, *Phys. Rev. B* **1974**, *10*, 1642.
[36] A. Shchepetilnikov, A. Zarezin, V. Muravev, P. Gusikhin, I. Kukushkin, *Opt. Eng.* **2020**, *59*, 061617.
[37] C. Shannon, *Proc. IRE* **1949**, *37*, 10.
[38] B. Gompf, M. Gerull, T. Muller, M. Dressel, *Infrared Phys. Technol.* **2006**, *49*, 128.
[39] B. Terris, H. Mamin, D. Rugar, *Appl. Phys. Lett.* **1996**, *68*, 141.
[40] B. Terris, H. Mamin, D. Rugar, W. Studenmund, G. Kino, *Appl. Phys. Lett.* **1994**, *65*, 388.
[41] G. Tessier, M. Bardoux, C. Bouue, C. Filloy, D. Fournier, *Appl. Phys. Lett.* **2007**, *90*, 171112.
[42] N. Chernomyrdin, A. Schadko, S. Lebedev, V. Tolstoguzov, V. Kurlov, I. Reshetov, I. Spektor, M. Skorobogatiy, S. Yurchenko, K. Zaytsev, *Appl. Phys. Lett.* **2017**, *110*, 221109.
[43] D. Fletcher, *Microscale Thermophys. Eng.* **2003**, *7*, 267.
[44] Q. Wu, R. Grober, D. Gammon, D. Katzer, *Phys. Rev. Lett.* **1999**, *83*, 2652.
[45] S. Bishop, J. Hadden, R. Hekmati, *Appl. Phys. Lett.* **2022**, *120*, 114001.
[46] A. Pimenov, A. Loidl, *Appl. Phys. Lett.* **2003**, *83*, 4122.
[47] S. Ippolito, S. Thorne, M. Eraslan, B. Goldberg, M. Unlu, Y. Leblebici, *Appl. Phys. Lett.* **2004**, *84*, 4529.
[48] K. Karrai, X. Lorenz, L. Novotny, *Appl. Phys. Lett.* **2000**, *77*, 3459.
[49] D. Fletcher, K. Crozier, C. Quate, G. Kino, K. Goodson, D. Simanovskii, D. Palanker, *Appl. Phys. Lett.* **2001**, *78*, 3589.
[50] E. Ramsay, N. Pleynet, D. Xiao, R. Warburton, D. Reid, *Opt. Lett.* **2005**, *30*, 26.
[51] D. Fletcher, K. Crozier, K. Guarini, S. Minne, G. Kino, C. Quate, K. Goodson, *J. Microelectromech. Syst.* **2001**, *10*, 450.
[52] D. Fletcher, K. Crozier, C. Quate, G. Kino, K. Goodson, D. Simanovskii, D. Palanker, *Appl. Phys. Lett.* **2000**, *77*, 2109.
[53] F. H. Köklü, J. I. Quesnel, A. N. Vamivakas, S. B. Ippolito, B. B. Goldberg, M. S. Ünlü, *Opt. Express* **2008**, *16*, 9501.
[54] E. M. Khabushev, D. V. Krasnikov, O. T. Zaremba, A. P. Tsapenko, A. E. Goldt, A. G. Nasibulin, *J. Phys. Chem. Lett.* **2019**, *10*, 6962.
[55] G. Katyba, N. Raginov, E. Khabushev, V. Zhelnov, A. Gorodetsky, D. Ghazaryan, M. Mironov, D. Krasnikov, Y. Gladush, J. Lloyd-Hughes, A. Nasibulin, A. Arsenin, V. Volkov, K. Zaytsev, M. Burdanova, *Optica* **2023**, *10*, 53.
[56] Z. Yan, L.-G. Zhu, K. Meng, W. Huang, Q. Shi, *Trends Biotechnol.* **2022**, *40*, 816.
[57] C. D. Stoik, M. J. Bohn, J. L. Blackshire, *Opt. Express* **2008**, *16*, 17039.
[58] J. True, C. Xi, N. Jessurun, K. Ahi, N. Asadizanjani, *Opt. Eng.* **2021**, *60*, 060901.
[59] J. A. Zeitler, P. F. Taday, D. A. Newnham, M. Pepper, K. C. Gordon, T. Rades, *J. Pharm. Pharmacol.* **2010**, *59*, 209.
[60] A. Ren, A. Zahid, D. Fan, X. Yang, M. A. Imran, A. Alomainy, Q. H. Abbasi, *Trends Food Sci. Technol.* **2019**, *85*, 241.
[61] A. Kucheryavenko, V. Zhelnov, D. Melikyants, N. Chernomyrdin, S. Lebedev, V. Bukin, S. Garnov, V. Kurlov, K. Zaytsev, G. Katyba, *Opt. Express* **2023**, *31*, 13366.
[62] G. Komandin, V. Anzin, V. Ulitko, A. Gavdush, A. Mukhin, Y. Goncharov, O. Porodinkov, I. Spektor, *Opt. Eng.* **2019**, *59*, 061603.
[63] D. Lavrukhin, A. Yachmenev, A. Pavlov, R. Khabibullin, Y. Goncharov, I. Spektor, G. Komandin, S. Yurchenko, N. Chernomyrdin, K. Zaytsev, D. Ponomarev, *Semicond. Sci. Technol.* **2019**, *34*, 034005.
[64] G. Musina, I. Dolganova, N. Chernomyrdin, A. Gavdush, V. Ulitko, O. Cherkasova, D. Tuchina, P. Nikitin, A. Alekseeva, N. Bal, G. Komandin, V. Kurlov, V. Tuchin, K. Zaytsev, *J. Biophotonics* **2020**, *13*, 202000297.
[65] I. Pupeza, R. Wilk, M. Koch, *Opt. Express* **2007**, *15*, 4335.
[66] K. Zaytsev, A. Gavdush, V. Karasik, V. Alekhnovich, P. Nosov, V. Lazarev, I. Reshetov, S. Yurchenko, *J. Appl. Phys.* **2014**, *115*, 193105.
[67] A. Cangellaris, *Proc. of Symp. on Electromagnetic Compatibility*, IEEE, Piscataway, NJ **1996**, pp. 107–116.
[68] V. Tuchin, *Tissue Optics: Light Scattering Methods and Instruments for Medical Diagnostics*, 3rd ed., SPIE Press, Bellingham, WA **2015**.
[69] L. Oliveira, K. Zaytsev, V. Tuchin, *Proc. SPIE* **2020**, *11585*, 1158503.
[70] I. Martins, H. Silva, E. Lazareva, N. Chernomyrdin, K. Zaytsev, L. Oliveira, V. Tuchin, *Biomed. Opt. Express* **2023**, *14*, 249.
[71] G. Musina, A. Gavdush, N. Chernomyrdin, I. Dolganova, V. Ulitko, O. Cherkasova, V. Kurlov, G. Komandin, I. Zhivotovskii, V. Tuchin, K. Zaytsev, *Opt. Spectrosc.* **2020**, *128*, 1026.